

# Proposed Lunar Measurements of $r$ -Process Radioisotopes to Distinguish Origin of Deep-sea $^{244}\text{Pu}$

Xilu Wang<sup>a,b,c,1</sup>, Adam M. Clark<sup>c</sup>, John Ellis<sup>d,e</sup>, Adrienne F. Ertel<sup>f,g</sup>, Brian D. Fields<sup>f,g,h</sup>, Brian J. Fry<sup>i</sup>, Zhenghai Liu<sup>f</sup>, Jesse A. Miller<sup>f,g</sup>, and Rebecca Surman<sup>c</sup>

<sup>a</sup>Key Laboratory of Particle Astrophysics, Institute of High Energy Physics, Chinese Academy of Sciences, Beijing, 100049, China; <sup>b</sup>N3AS Collaboration, Department of Physics, University of California, Berkeley, CA 94720, USA; <sup>c</sup>Department of Physics and Astronomy, University of Notre Dame, Notre Dame, IN 46556, USA; <sup>d</sup>Theoretical Physics and Cosmology Group, Department of Physics, King's College London, Strand, London WC2R 2LS, UK; <sup>e</sup>NICPB, Ravala pst. 10, 10143 Tallinn, Estonia; <sup>f</sup>Theoretical Physics Department, CERN, CH-1211 Geneva 23, Switzerland; <sup>g</sup>Department of Astronomy, University of Illinois, Urbana, IL 61801, USA; <sup>h</sup>Illinois Center for the Advanced Study of the Universe, University of Illinois, Urbana, IL 61820, USA; <sup>i</sup>Department of Physics, University of Illinois, Urbana, IL 61801, USA; <sup>1</sup>Department of Physics, United States Air Force Academy, Colorado Springs, CO 80840, USA

**$^{244}\text{Pu}$  has recently been discovered in deep-sea deposits spanning the past 10 Myr, a period that includes two  $^{60}\text{Fe}$  pulses from nearby supernovae.  $^{244}\text{Pu}$  is among the heaviest  $r$ -process products, and we consider whether it was created in the supernovae, which is disfavored by nucleosynthesis simulations, or in an earlier kilonova event that seeded  $^{244}\text{Pu}$  in the nearby interstellar medium that was subsequently swept up by the supernova debris. We discuss how these possibilities can be probed by measuring  $^{244}\text{Pu}$  and other  $r$ -process radioisotopes such as  $^{129}\text{I}$  and  $^{182}\text{Hf}$ , both in lunar regolith samples returned to Earth by missions such as *Chang'e* and *Artemis*, and in deep-sea deposits.**

$r$ -Process | Kilonovae | Supernovae | Lunar regolith | Accelerator Mass Spectrometry

Measurements of live radioactive isotopes can provide insights into recent astrophysical explosions such as core-collapse supernovae (SNe) within  $\mathcal{O}(100)$  pc of Earth (1) that are expected to occur every few million years, clarifying the possibility of rarer events within  $\mathcal{O}(10)$  pc that might have caused mass extinctions in the past (2, 3). Many experiments over the past two decades have detected pulses of live  $^{60}\text{Fe}$  in deep-sea deposits (4–9) from between 2 and 3 My ago (Mya), very likely due to a nearby core-collapse SN. There have also been measurements of  $^{60}\text{Fe}$  in the lunar regolith (10), in cosmic rays (11) and in Antarctic snow (12).

These measurements were accompanied by some tantalizing hints of deep-sea  $^{244}\text{Pu}$  (13–16). These are interesting because the  $^{244}\text{Pu}$  is produced exclusively by the astrophysical rapid neutron capture process ( $r$ -process), which is one of the dominant avenues to synthesize elements heavier than iron in the Universe (17). The nature of the  $r$ -process lies at the heart of multi-messenger astronomy, with connections to gravitational wave observations and gamma-ray bursts (18–21), as well as observations of the most ancient stars (22–24). The nuclear physics of the  $r$ -process demands that an intense neutron flux act over a short timescale  $\sim 1$  sec; this points to explosive conditions (17). The astrophysical sites that most plausibly host such conditions are core-collapse supernovae and neutron star mergers (kilonovae): see the reviews (25–28) and references therein. Which of these dominated production in the early Galaxy, and which dominates today, remains frustratingly difficult to identify unambiguously, in part because  $r$ -process observables such as abundance patterns potentially sum contributions from multiple events.

Deep-sea samples open a new window on the  $r$ -process,

and are particularly exciting because they give information on specific isotopes (not elemental sums), and they sample ejecta from a single event (29). Motivated by these hints, in an earlier paper we studied possible signatures of SN and KN  $r$ -process events, analyzing the potential implications of  $^{244}\text{Pu}$  detection, estimating the strengths of other  $r$ -process radioisotope signatures, and discussing how they could help distinguish between potential sites (29).

A major advance in studies of live astrophysical radioisotopes has recently been made by Wallner et al. in ref. (30) with the discovery  $^{244}\text{Pu}$  in deep-sea ferromanganese (Fe-Mn) crusts from periods that include both this and the  $\sim 3$  Mya  $^{60}\text{Fe}$  pulse. Whereas earlier hints had reported single  $^{244}\text{Pu}$  atoms, ref. (30) reported  $181 \pm 19$  atoms above background, indicating a firm detection. This same study also found an earlier  $^{60}\text{Fe}$  pulse  $\sim 7$  Mya. These results add new dimensions to our picture of recent near-Earth explosions, and widen the scope of their implications. Broadly, the detection of  $^{244}\text{Pu}$  is not only the second firmly detected radioisotope in this epoch, but also demands an  $r$ -process source and so probes the astrophysical site of the  $r$  process. Further, the second  $^{60}\text{Fe}$  pulse shows that there were multiple explosions, as one

## Significance Statement

The rapid neutron capture process ( $r$ -process) is a dominant avenue for heavy-element synthesis but its astrophysical sites remain a mystery. We respond to the recent detection of live  $^{244}\text{Pu}$  deposited on Earth during the past 10 Myr, which opens a qualitatively new vista onto the  $r$ -process,  $^{244}\text{Pu}$  being the heaviest  $r$ -process species ever detected. We quantify the consequences of competing supernova and kilonova interpretations that directly illuminate the elusive  $r$ -process site. We propose new lunar and other measurements that could distinguish these possibilities. This paper opens new avenues in a central area of astrophysics and nuclear physics, links near-Earth explosions and the  $r$ -process, and offers new science opportunities for lunar sample returns.

X.W. is the main contributor to the theoretical calculations, measurement data collection and analysis. B.D.F. participated in the theoretical calculations and data analysis. R.S., J.E. and B.J.F. participated in the theory interpretation and discussions. A.M.C. contributed to the experiment discussions. X.W., A.M.C., J.E., B.D.F. and R.S. participated in the writing and editing of the paper. All other authors participated in general reviews of the paper.

The authors declare no competing interests.

<sup>1</sup>To whom correspondence should be addressed. E-mail: wangxl@ihep.ac.cn

would expect from massive stars that are highly clustered (31). We thus follow (32) in referring to the event around 3 Mya as the Pliocene event (SN Plio) and the event around 7 Mya as the Miocene event (SN Mio). In this paper we study the interpretation and potential implications of these new experimental results, focusing on the information to be gained from lunar measurements of  $r$ -process radioisotopes.

As has been shown in (33), ordinary (non- $r$ -process) nucleosynthesis in core-collapse SNe provides the only plausible source of  $^{60}\text{Fe}$  observed in the two pulses. Ref. (30) concurs, making this a starting point of its analysis. The question then becomes: *could either or both of these SNe also have produced the  $^{244}\text{Pu}$ , or is a separate event required, presumably a KN?*

The two  $^{60}\text{Fe}$  pulses require at least two distinct SNe. The  $^{244}\text{Pu}$  data were not sampled as finely in time as the  $^{60}\text{Fe}$  data, but in three broad time windows including a surface layer that includes anthropogenic contamination. The two deeper layers each overlap with a  $^{60}\text{Fe}$  pulse, with similar  $^{60}\text{Fe}/^{244}\text{Pu}$  ratios, represented by the yellow band in Fig. 1. The data show  $^{60}\text{Fe}$  to be much more abundant than  $^{244}\text{Pu}$  in both pulses. Here we confront these new data with the supernova and neutron-star merger nucleosynthesis models developed in (29) and explore the prospects of fresh measurements that might discriminate between possible scenarios, emphasizing the value of analyzing lunar regolith samples returned to Earth by missions such as *Chang'e* and *Artemis*.

**SNe and KNe models of  $^{60}\text{Fe}$  and  $^{244}\text{Pu}$ .** The astrophysical origins of  $r$ -process elements including the actinides have been the subject of considerable debate (27). SNe may produce the  $r$ -process either via a neutrino-driven wind or in magnetohydrodynamic (MHD) jets, but both mechanisms struggle to make actinides, see (29) and references therein. If SNe are confirmed as robust sources of actinides such as  $^{244}\text{Pu}$ , the available models must have major omissions. Neutron-star mergers that lead to KN explosions, on the other hand, have been observed to produce  $r$ -process species such as lanthanides (19) and are expected to produce actinides (27), though the latter has yet to be confirmed observationally (34).

In (29) we constructed four SN and KN models to examine  $r$ -process radioisotope production. Our two models featured a modified neutrino-driven wind (35) scenario *forced* to produce actinides, denoted by  $\nu^*$  (SA), and a high magnetic field MHD SN model (36), denoted by SB, both with  $r$ -process nucleosynthesis constrained using data on the metal-poor star HD160617 (22). For neutron star mergers we explored two combinations of calculations of neutron-star merger dynamical ejecta (37) and a disk  $\nu$ -driven wind (38), constrained to fit data on either HD160617 (KA) or the actinide-boost star J0954+5246 (23) (KB). Details of these models are found in (29).

The  $^{60}\text{Fe}/^{244}\text{Pu}$  ratios for the four models of  $r$ -process production are compared to the data from (30) in Fig. 1. In the SA and SB models, the  $^{60}\text{Fe}$  production is underestimated, as SNe produce  $^{60}\text{Fe}$  during hydrostatic burning phases and during the explosion (39–42), apart from any potential  $r$ -process contribution. Hence, in order to compare our models to the new data from (30), we need to consider sources of  $^{60}\text{Fe}$  within the SN event in addition to the  $r$ -process yields from (29). Our procedure to do this appears in the Materials and Methods section.

We see that either of the SN models SA or SB could ac-

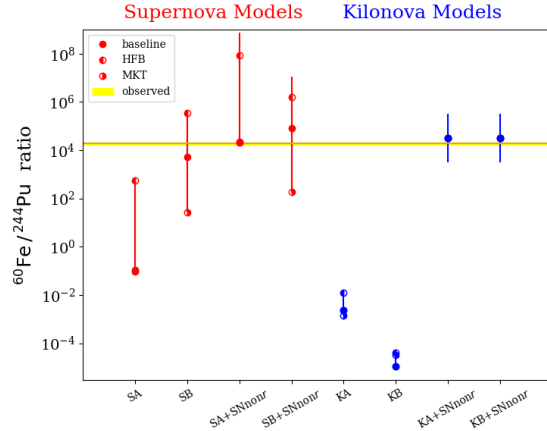


**Fig. 1.** The  $^{60}\text{Fe}/^{244}\text{Pu}$  abundance ratios calculated (29) in forced  $\nu$  wind and MHD SN models (SA and SB), and in KN models (KA and KB). We present results for each model both without and including an additional non- $r$ -process SN source of  $^{60}\text{Fe}$  at 100 pc; calculations are for events 3 Mya, but with a 10 Mya kilonova in the two-step KA/B+SNeor models. The yellow band indicates the observed  $^{60}\text{Fe}/^{244}\text{Pu}$  ratio (30) for 3 Mya (SN Plio). The error bars indicating the impact  $r$ -process nuclear uncertainties discussed in the Materials and Methods: filled symbols are the baseline FRDM+QRPA nuclear model, while the left (right) half-filled symbols are the HFB (MKT) models.

commodate the (similar)  $^{60}\text{Fe}/^{244}\text{Pu}$  ratios reported by (30) in the periods around 3 and 7 Mya. On the other hand, both the KN models KA and KB predict much smaller  $^{60}\text{Fe}/^{244}\text{Pu}$  ratios, even when the uncertainties are taken into account. We therefore conclude that the  $^{60}\text{Fe}$  pulses and  $^{244}\text{Pu}$  detection *cannot be due to KN explosions alone*, at least as described by the models considered here.

We consider now the data of (30) on the  $^{60}\text{Fe}$  pulse from  $\sim 3$  Mya. The timing of this signal is consistent with that measured previously in  $^{60}\text{Fe}$  deposits in deep-sea sediments and crusts (4–9), though this peak is somewhat broader. The observed amplitude of the pulse and its duration  $\gtrsim 1$  Myr are consistent with a model in which  $^{60}\text{Fe}$  from a SN 100 pc away is transported to Earth in dust grains via ‘pinball’ trajectories that are deflected and trapped by a magnetic field within the SN remnant (32, 43). The pulse width indicated by the (30) measurements could also reflect smearing in the crust they study. Accordingly, we assume that this pulse was produced by a single SN.

In our SN models, we also make the economical assumption that the  $^{244}\text{Pu}$  from  $\leq 4.57$  Mya measured by (30) is also associated with SN Plio 3 Myr ago. We emphasize that observations with finer timing resolution would be needed to confirm this association, but note that many of our comments below would apply also if it were due to two or more SNe. As discussed above, the additional  $^{60}\text{Fe}$  peak discovered by (30), see also Fig. 1 of (6), is likely due to another SN that occurred  $\sim 7$  Mya (SN Mio), also some  $\sim 100$  pc away. We assume that all the  $^{244}\text{Pu}$  from 4.57 to 9 Mya measured by (30) is associated with this SN explosion, while emphasizing that observations with finer timing resolution would also be needed to confirm this association. Under this assumption, the  $^{244}\text{Pu}/^{60}\text{Fe}$  ratios in the ejecta of the two SNe  $\sim 3$  and  $\sim 7$  Mya are comparable within a factor  $\sim 2$  and indistinguishable in Fig. 1.

This is intriguing, since simulations indicate that only very specific types of SN can make much  $^{244}\text{Pu}$  (29), in which

case seeing two of them looks like a remarkable coincidence. If such an interpretation were correct, it would suggest not only that many or most SNe are  $r$ -process sites, but also that their production extends all the way to the actinides. If this could be established, standard  $\nu$ -driven wind and MHD models must have major omissions. That said, actinide production is possible in the *forced* neutrino wind and MHD models  $\nu^*$  (SA) and SB discussed in (29).

Nevertheless, there are serious potential issues for scenarios with actinide production in many or most SNe, provided by measurements of the  $r$ -process abundances in metal-poor stars. (a) It is known that  $r$ -process/Fe ratios (estimated using Eu/Fe as a proxy) vary wildly, with most stars showing low values and only a minority showing high values (44). The obvious interpretation is that Fe and  $r$ -process production are decoupled. If SNe do indeed make the  $r$ -process, one possibility would be that (core-collapse) supernova Fe production is highly variable. However, there are observational constraints on this from observations of SN light curves powered by  $^{56}\text{Ni}$  decay, so it seems more likely that the variations in  $r$ -process/Fe ratios are due to variations in  $r$ -process production. Another issue is that (b) searches for  $r$ -process species in metal-poor dwarf galaxies found them only in  $\sim 10\%$  (45). This strongly suggests that  $r$ -process events are much rarer than SNe. An alternative hypothesis is that the  $r$ -process material is ejected preferentially from the dwarf galaxies, e.g., in jets, but in this case jets would have to be features of most SNe, which is not supported by observations.

Motivated by these considerations, we proposed in (29) that  $^{244}\text{Pu}$  signals could arise via a two-step process in which material deposited previously in the interstellar medium (ISM) by an earlier KN was then swept up by subsequent SN explosions\*. Estimates of the KN rate in the Galaxy are compatible with a KN explosion  $\mathcal{O}(300)$  pc away that occurred  $\mathcal{O}(10)$  Mya. Accordingly, we also show in Fig. 1 results from models in which the debris from a KN explosion 10 Mya is mixed with the  $^{60}\text{Fe}$  of SN Plio 3 Mya. This two-step model discussed in ref. (29) is consistent with the data shown in Fig. 1, and could explain naturally the similarity between the  $^{244}\text{Pu}/^{60}\text{Fe}$  ratios in the periods covering the two  $^{60}\text{Fe}$  pulses found by (30).

**Deep-sea measurements.** Figure 1 suggests that the current  $^{60}\text{Fe}$  and  $^{244}\text{Pu}$  data on their own are insufficient to discriminate between the SN-only estimates and the two-step KN/SN scenario, so we consider also the possibility of observing additional SNe pulses in deep-sea deposits from  $> 7$  Mya. A model of the Local Bubble and  $^{60}\text{Fe}$  transport proposed in (46, 47) postulates 14 to 20 SNe in the Scorpius-Centaurus (Sco-Cen) stellar association within 300 pc over the past 13 My, among which might be progenitors for the two observed  $^{60}\text{Fe}$  pulses. Ref. (30) reported the results of  $^{60}\text{Fe}$  searches extending over the past 10 Myr, finding that the signal-to-background ratio for  $^{60}\text{Fe}$  falls to around unity for deposits from between 7 and 10 Mya. The relatively short  $^{60}\text{Fe}$  half-life of 2.6 My would make searches for earlier  $^{60}\text{Fe}$  pulses even more challenging. On the other hand, indirect evidence for earlier SNe could come from pulses of swept-up  $^{244}\text{Pu}$  in earlier deep-sea deposits, in view of its much longer half-life  $\sim 80$  My. Ref. (16) reported the results of a search for  $^{244}\text{Pu}$  extending over the past 25 My, finding one event from  $> 12$  Mya. This event

might just be background, but if not would correspond to a rate of deposition similar to that between 5 and 12 Mya. The more sensitive  $^{244}\text{Pu}$  results of (30) extend back to 9 Mya, and it would clearly be interesting to extend the search for an earlier  $^{244}\text{Pu}$  signal and any possible time structure.

**Additional radioisotopes of interest.** Another, potentially more powerful, way to distinguish between the possible production scenarios is to look for other radioisotopes present alongside the  $^{60}\text{Fe}$  and  $^{244}\text{Pu}$ . Any  $r$ -process mechanism that produces  $^{244}\text{Pu}$  also produces many other radioisotopes, not only other actinides such as  $^{236}\text{U}$ ,  $^{237}\text{Np}$ , and  $^{247}\text{Cm}$ , but also many other radioisotopes with masses intermediate between  $^{244}\text{Pu}$  and  $^{60}\text{Fe}$ . Hence their abundances would in general exhibit pulses coincident with the two SN  $^{60}\text{Fe}$  pulses, whether the  $r$ -process location is a recent, nearby SN or an earlier, more distant KN. However, the relative abundances of the peaks of different  $r$ -process isotopes would be affected by their lifetimes, which would help distinguish scenarios in which the  $r$ -process occurred at different times in the past.

We have calculated the relative abundances of live  $r$ -process radioisotopes produced by the *forced*  $\nu$ -wind (SA) and MHD (SB) models for SN Plio and Mio that occurred 3 Mya and 7 Mya discussed above, as well as two scenarios with a KN explosion 10 or 20 Mya. If the  $^{244}\text{Pu}$  measured in (30) was produced by such a SN, one could hope to see accompanying signals of  $r$ -process production of the radioisotopes  $^{93}\text{Zr}$ ,  $^{107}\text{Pd}$ ,  $^{129}\text{I}$ ,  $^{135}\text{Cs}$ ,  $^{182}\text{Hf}$ ,  $^{236}\text{U}$ , and possibly  $^{237}\text{Np}$  and  $^{247}\text{Cm}$ , as listed in Table 1. The first four columns of Table 1 compare the yields of live  $r$ -process radioisotopes predicted by SN models SA and SB for SNe that exploded 3 and 7 Mya. We emphasize that the  $^{60}\text{Fe}/^{244}\text{Pu}$  ratios given in this Table are only for  $^{60}\text{Fe}$  produced via the  $r$ -process, and that we would expect these SNe to produce much more  $^{60}\text{Fe}$  via the standard neutron capture mechanism. The last four columns in Table 1 show results from calculations of  $r$ -process isotope production in KN models KA and KB, assuming an event 10 or 20 Mya, bracketing the formation of the Local Bubble. In this case many of the shorter-lived radioisotopes that could have been detectable in the SN scenario would have decayed away, and we find that if the measured  $^{244}\text{Pu}$  was produced by a KN 10 or 20 Mya, the best prospect for detection (with the biggest radioisotope ratio to  $^{244}\text{Pu}$ ) is for  $^{129}\text{I}$ .

Figure 2 compares the total yields of selected live  $r$ -process radioisotopes predicted by our SN and KN models with direct deposition (one-step) as well as two-step scenario (a 10 Mya KN plus a 3 Mya non- $r$ -process SN), with similar calculations as in Fig. 1. We highlight in Fig. 2 representative isotopes in each of the three regions of the  $r$ -process abundance pattern, namely  $^{93}\text{Zr}$ ,  $^{129}\text{I}$ , and  $^{182}\text{Hf}$ , which we now discuss in turn.  $^{93}\text{Zr}$  can be produced in an alpha-rich freezeout of mildly neutron-rich supernova ejecta without an accompanying main  $r$ -process, so its detection could be a probe of this additional nucleosynthetic source. Here we take the non- $r$ -process SN  $^{93}\text{Zr}$  yields to be  $M_{\text{ej},93} \sim 10^{-7.5} M_{\odot}$  (see Materials and Methods). As for  $^{129}\text{I}$ , our predictions show that it should be detectable alongside  $^{244}\text{Pu}$  in any scenario, with measurement of the ratio offering possibly the strongest discrimination between scenarios. Finally, we anticipate that  $^{182}\text{Hf}$  could be a clear marker of prompt supernova production, as it is present in potentially detectable levels for the SA and SB models, but not in the two-step kilonova scenarios.

\*First estimates of the possible amounts of swept-up  $^{60}\text{Fe}$  and  $^{244}\text{Pu}$  were given in (1).



**Table 1.** *r*-process isotope ratios in *forced* SN models for explosions 3/7 Mya, corresponding to the known  $^{60}\text{Fe}$  pulses, and in KN models for explosions 10/20 Mya, bracketing the formation of the Local Bubble.

Radioisotope Ratio	Supernova Models				Kilonova Models			
	SA		SB		KA		KB	
	3 Mya	7 Mya	3 Mya	7 Mya	10 Mya	20 Mya	10 Mya	20 Mya
$^{60}\text{Fe}/^{244}\text{Pu}$	$9.2 \times 10^{-2}$	$3.2 \times 10^{-2}$	$5.3 \times 10^3$	$1.8 \times 10^3$	$3.7 \times 10^{-4}$	$3.0 \times 10^{-5}$	$1.7 \times 10^{-6}$	$1.4 \times 10^{-7}$
$^{93}\text{Zr}/^{244}\text{Pu}$	5.2	0.93	$8.2 \times 10^4$	$1.5 \times 10^4$	0.24	$3.6 \times 10^{-3}$	$7.7 \times 10^{-3}$	$1.2 \times 10^{-4}$
$^{107}\text{Pd}/^{244}\text{Pu}$	52	35	$1.3 \times 10^5$	$8.6 \times 10^4$	3.7	1.4	0.34	0.13
$^{129}\text{I}/^{244}\text{Pu}$	$3.2 \times 10^2$	$2.8 \times 10^2$	$1.7 \times 10^6$	$1.5 \times 10^6$	69	49	14	10
$^{135}\text{Cs}/^{244}\text{Pu}$	5.4	0.68	$1.2 \times 10^5$	$1.5 \times 10^4$	$8.7 \times 10^{-3}$	$5.5 \times 10^{-5}$	$3.7 \times 10^{-2}$	$2.4 \times 10^{-4}$
$^{182}\text{Hf}/^{244}\text{Pu}$	3.1	2.3	$4.4 \times 10^3$	$3.3 \times 10^3$	0.43	0.22	$6.9 \times 10^{-2}$	$3.5 \times 10^{-2}$
$^{236}\text{U}/^{244}\text{Pu}$	1.8	1.7	9.5	8.7	1.8	1.5	1.0	0.92
$^{237}\text{Np}/^{244}\text{Pu}$	0.66	0.18	1.6	0.43	$8.2 \times 10^{-2}$	$3.7 \times 10^{-3}$	$5.6 \times 10^{-2}$	$2.5 \times 10^{-3}$
$^{247}\text{Cm}/^{244}\text{Pu}$	0.50	0.43	0.45	0.39	0.38	0.27	0.35	0.25

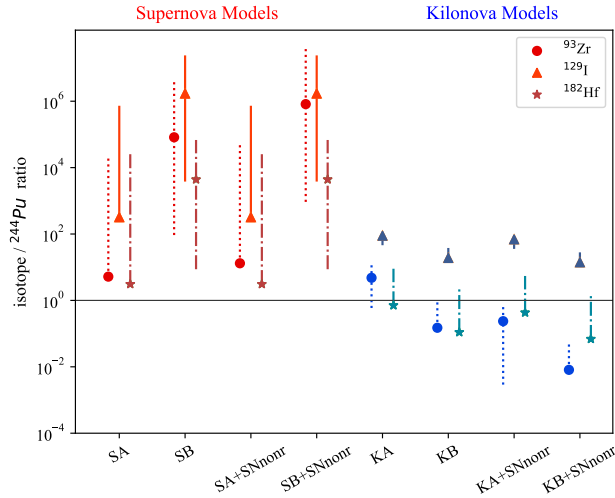


**Fig. 2.** Ratios to  $^{244}\text{Pu}$  of the selected live *r*-process radioisotopes  $^{93}\text{Zr}$ ,  $^{129}\text{I}$  and  $^{182}\text{Hf}$ , calculated in a similar way to Fig. 1.

It is a common feature of all the SN and KN models studied above that the best prospects for discovering a second live *r*-process radioisotope (in addition to  $^{244}\text{Pu}$ ) may be offered by  $^{129}\text{I}$ . The  $^{129}\text{I}/^{244}\text{Pu}$  ratio calculated in the models we have studied ranges from  $\mathcal{O}(10)$  in the KN models through  $\mathcal{O}(100)$  in SN model SA to  $\mathcal{O}(10^6)$  in SN model SB, thereby offering the possibility of distinguishing between scenarios. An  $^{129}\text{I}/^{244}\text{Pu}$  ratio exceeding  $10^5$  that is coincident with either of the observed SN pulses would favour SN model SB, which would also predict  $^{182}\text{Hf}/^{244}\text{Pu}$  ratios  $> 10^3$ . On the other hand, a  $^{129}\text{I}/^{244}\text{Pu}$  ratio between  $10^3$  and 10 could be accommodated by any of the models SA, KA and KB. In this case, model SA suggests that  $^{182}\text{Hf}$  might be present at levels similar to  $^{244}\text{Pu}$ , whereas the KN models predict smaller ratios for  $^{182}\text{Hf}$  relative to  $^{244}\text{Pu}$ , that are less likely to be detectable. Hence, detection of  $^{182}\text{Hf}$  at a level similar to  $^{244}\text{Pu}$  would point strongly towards a SN *r*-process origin. Additionally, detection of any of the other *r*-process radioisotopes  $^{93}\text{Zr}$ ,  $^{107}\text{Pd}$ ,  $^{135}\text{Cs}$ ,  $^{182}\text{Hf}$ ,  $^{237}\text{Np}$  or  $^{247}\text{Cm}$  would favour a SN origin for the  $^{244}\text{Pu}$ . A  $^{236}\text{U}$  signal is possible in both the SN and KN scenarios, but may suffer from anthropogenic or natural backgrounds in which  $^{235}\text{U}$  can capture a neutron.

**Lunar regolith searches.** Lunar regolith (soil) serves as a natural archive for material from nearby explosions that is comple-

mentary to terrestrial samples. Advantages of lunar archives include the geological inactivity of the Moon, the lack of an atmosphere or oceans that can redistribute material, and the lack of anthropogenic disturbances or contamination. On the other hand, the lunar surface is slowly reworked by meteoritic “gardening” (48, 49), so signals from multiple events will be mixed. Moreover, the lunar surface is unshielded from cosmic rays, which create a background of radioisotopes in the regolith (50–53). Any supernova or kilonova signal must stand out from this background in order to be detectable. Here we focus on the detectability of live *r*-process radioisotopes on the Moon.

Lunar regolith samples come at a great cost, but our inventory will soon increase dramatically beyond the *Apollo* and *Luna* samples that date back to the 1960’s and 1970’s. The robotic *Chang’e-5* mission (54) has recently delivered a  $\sim 1.7$  kg sample from a location farther north than any prior landings, the *Chang’e-6* mission will land in the South Pole region of the Moon in 2024, and the upcoming crewed *Artemis* mission (55) will bring back  $\sim 100$  kg of samples in the initial landing near the South Pole, with more planned thereafter.

We recall that the discovery of  $^{60}\text{Fe}$  in several *Apollo* samples was reported in (10). The data of (30) suggest that this  $^{60}\text{Fe}$  is likely to have originated from a combination of the  $^{60}\text{Fe}$  pulses from 3 and 7 Mya, mainly the more recent pulse in view of its greater fluence and younger age. Confirmation of this  $^{60}\text{Fe}$  signal, e.g., in the sample returned recently by the *Chang’e-5* mission (54) or that from a future *Artemis* lunar landing mission (55), would require analyzing a modest sample of  $\lesssim 100$  mg of lunar material <sup>†</sup>.

The detection of  $^{244}\text{Pu}$  in the deep sea implies that a corresponding lunar signal must exist as well. Any cosmic-ray background for  $^{244}\text{Pu}$  must arise from the available  $^{235}\text{U}$  and  $^{238}\text{U}$  targets. These require multiple *p* and *n* captures, and even then the  $\sim 5$  hour half-life of  $^{243}\text{Pu}$  effectively diverts any cosmogenic flow away from  $^{244}\text{Pu}$ . Cosmic rays can also destroy  $^{244}\text{Pu}$  by neutron capture, but this effect is negligible compared to decay: in the Materials and Methods, we estimate  $\Gamma_{244+n\tau_{244}} \sim 4 \times 10^{-8} \ll 1$ . We therefore conclude that cosmic-ray processes do not build up any appreciable  $^{244}\text{Pu}$  background in the regolith nor do they destroy it.  $^{244}\text{Pu}$

<sup>†</sup> Employing the regolith gardening model of (49, 56), it is estimated in (54) that the depth  $\Lambda$  at which the probability of at least one overturn is 99% is  $3.45 \times 10^{-5} t_{\text{yr}}^{0.47}$  m, where  $t_{\text{yr}}$  is the reworking time in years. This leads to  $\Lambda = 3.8$  (5.7) cm for material deposited 3 (7) Mya.

should thus be a particularly clean lunar target, as long as return samples are protected from terrestrial contamination.

In the deep-sea Fe-Mn crust, the relative abundance of  $^{244}\text{Pu}$  reported by (30) is  $^{244}\text{Pu}/^{60}\text{Fe} \sim 5 \times 10^{-5}$ . Since it is expected that uptake on the lunar surface is as efficient as in the deep-sea case, if not more, we anticipate sample sizes of similar mass ( $\sim 10$  g) would be needed to discover a  $^{244}\text{Pu}$  signal.

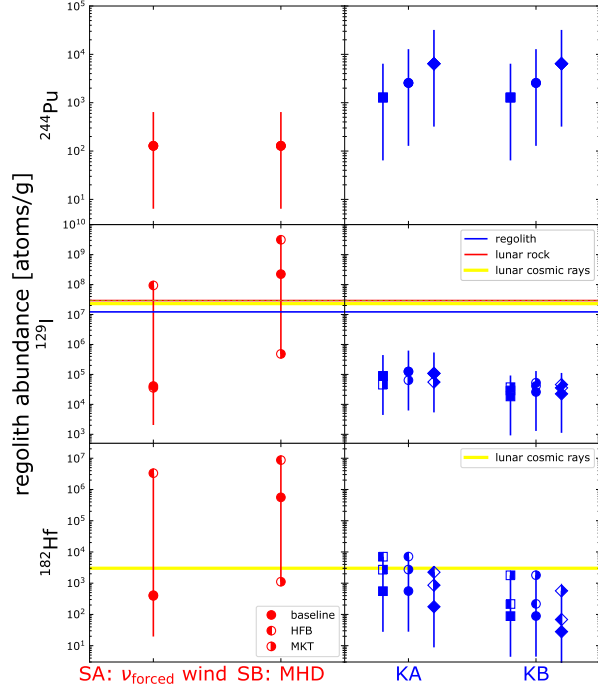


**Fig. 3.** Expected abundances of select  $r$ -process radionuclides in lunar regolith, based on  $^{244}\text{Pu}$  deep-ocean measurements. Points show predictions for SN and KN models, with error bars indicating the impact  $r$ -process nuclear uncertainties discussed in the Materials and Methods: filled symbols are the baseline FRDM+QRPA nuclear model, while the left (right) half-filled symbols are the HFB (MKT) models. For  $^{129}\text{I}$ , the horizontal blue and red lines show the levels measured in *Apollo* samples of lunar regolith (57) and rock (58), and the yellow line shows the calculated cosmic-ray background (For details of the cosmic-ray background estimations, see Materials and Methods). SN models are for an explosion 3 Myr ago; KN models show results for explosions 10, 20, and 50 Myr ago.

For other, lighter  $r$ -process radionuclides, the lunar regolith will contain a cosmogenic background that we must understand. Here we recommend the strategy that has successfully identified supernova  $^{60}\text{Fe}$  in lunar regolith in the presence of a cosmic-ray background (10), as discussed in Materials and Methods. A radionuclide  $i$  with a potential astrophysical signal will also have a cosmogenic component, so regolith abundances will sum the two, so we write the number per unit mass as  $y_i^{\text{obs}} = y_i^* + y_i^{\text{cr}}$ . The cosmogenic background in each part of the sample will depend on the cosmic-ray flux  $\Phi$  and the local target abundance:  $y_i^{\text{cr}} \propto \Phi y_{\text{target}|i}$ , where cosmic rays produce our species via  $\text{CR} + \text{target} \rightarrow i$ . The target abundance is directly observable in the return sample, but cosmic-ray flux is not. To infer the local cosmic-ray exposure

reliably requires the measurement of a radioisotope species  $j$  that is dominated by cosmic-ray production. This approach was used to measure supernova-produced  $^{60}\text{Fe}$  in the lunar regolith by also measuring  $^{53}\text{Mn}$  (10). Such a two-radioisotope “dyadic” approach (59) is elaborated in Materials and Methods, which shows that a plot of the ratio  $y_i^{\text{obs}}/y_j^{\text{obs}}$  as a function of the ratio of cosmic-ray targets  $y_{\text{target}|i}/y_{\text{target}|j}$  falls on a line if species  $i$  is cosmogenic only, while excursions above this line would indicate the presence of an additional extrasolar component.

While the  $r$ -process actinide radionuclides  $^{244}\text{Pu}$  and  $^{247}\text{Cm}$  will not have an appreciable cosmic-ray background, a substantial background will exist for  $^{236}\text{U}$  and  $^{237}\text{Np}$  which can be created from lunar  $^{235}\text{U}$ . Cosmogenic production will also be an issue for all of the lighter species we consider. Of the lighter species,  $^{93}\text{Zr}$ ,  $^{107}\text{Pd}$ , and  $^{135}\text{Cs}$  have abundant cosmogenic target nuclei in the regolith, which leads to prohibitively large backgrounds. We therefore focus on  $^{129}\text{I}$  and  $^{182}\text{Hf}$  where the background is smaller.

Table 2 summarizes the prospects for lunar detection of  $^{244}\text{Pu}$ , as well as for  $^{129}\text{I}$  and  $^{182}\text{Hf}$  including cosmogenic backgrounds estimated as described in the Materials and Methods section. We also estimate the minimum number  $N_{i,\text{min}}$  of atoms of each species needed for a confident accelerator mass spectrometry (AMS) measurement, based on present sensitivity levels and extraction efficiency. From the needed number of atoms and the predicted number  $y_i = n_i/\rho$  of signal atoms per gram, we estimate the sample mass  $m_{i,\text{min}} = N_{i,\text{min}}/y_i$  needed; for the SN case this spans a large range, reflecting the large uncertainties in the predictions.

The AMS sensitivity for  $^{129}\text{I}$  together with large  $^{129}\text{I}/^{244}\text{Pu}$  predicted ratios suggests that  $^{129}\text{I}$  detection is already within the grasp of present techniques (if care is taken to avoid contamination from anthropogenic sources); indeed, intriguing measurements already exist.  $^{129}\text{I}$  has already been detected in a Fe-Mn crust (60), showing a dropoff with depth consistent with a background source such as natural uranium fission. The Fe-Mn crust was not independently dated, but the abundance levels appear inconsistent with the SB model while allowing room for some SA models and the KA and KB models. We note that (61) used AMS to measure  $^{129}\text{I}$  in the lunar regolith, and (58) measured it in lunar rock, finding very similar abundances. Lunar rocks should not contain a SN or KN component so, at face value, these data seem to place an upper limit  $n(^{129}\text{I})/\rho \lesssim 3 \times 10^7$  atoms/g on any extrasolar signal. This result is consistent with the indications from  $^{129}\text{I}$  data in a Fe-Mn crust (62) discussed in (29). These measurements were not made with our research program in mind, but still the apparent non-detection of  $^{129}\text{I}$  puts pressure on the SN models, as seen in Fig. 3: it would rule out the HFB nuclear model for the forced neutrino wind case, as well as the baseline and HFB nuclear models for the MHD SN. Future dedicated  $^{129}\text{I}$  searches in the deep ocean and on the Moon would be of great interest.

Compared to  $^{129}\text{I}$ , current AMS capabilities offer less promise for detecting  $^{182}\text{Hf}$ . As estimated in Table 2, several kg of material may be required to detect a signal due to the limitations on AMS sensitivities caused by the interference from  $A = 182$  isobars. Due to the scarcity in available lunar material, higher sensitivity would be desirable to reduce the quantity that must be processed. Figure 3 motivates this

**Table 2. Lunar Regolith  $r$ -Process Radioisotopes From Near-Earth Explosions**

Isotope	Cosmic-Ray Targets	AMS Sensitivity		Sample Mass [g]	
		[atoms]	Background [atoms/g]	SN	KN
$^{129}\text{I}$	Te, Ba, La	$10^5$	$10^7$	$10^{-1} - 10^3$	1–10
$^{182}\text{Hf}$	$^{183}\text{W}$ , $^{184}\text{W}$ , $^{186}\text{W}$	$10^7$	$3 \times 10^3$	$2 - 5 \times 10^5$	$3 \times 10^3 - 10^6$
$^{244}\text{Pu}$	–	$10^2$	–	10	

effort, as the cosmic-ray production of  $^{182}\text{Hf}$  is predicted to be closer to the KN predictions than that of  $^{129}\text{I}$ . These data foreshadow the power of new radioisotope measurements on both terrestrial and lunar samples, particularly  $^{129}\text{I}$  and  $^{182}\text{Hf}$ , which can probe the nature of the recent explosions and of the  $r$ -process generally.

Finally, we note that the *spatial* distribution of  $^{60}\text{Fe}$  and other radioisotopes on the Moon carries information about the supernova direction and dust propagation (63). Over the long timescale of dust deposition, lunar rotation will average the deposition over longitude, but not latitude. Consequently the latitude distribution of radioisotopes probes the distribution of dust arrival directions. If the dust arrives in a plane wave, there will be pronounced gradients that should be detectable, but the extant *Apollo*  $^{60}\text{Fe}$  data is too uncertain to test for such a gradient (63). Future measurements of *Artemis* and *Chang'e* samples, particularly from landings near the lunar poles, could reveal the latitude distribution and thus give unique insight into the dust propagation. The results we show in Fig. 3 and Table 2 are for the latitude where a plane-wave flux arrives vertically; this will be modulated by the arrival direction distribution.

**Cosmic-ray measurements.** There are also possible signatures of nearby explosions in cosmic rays, including anomalies in positron and antiproton fluxes (64), and also in the ion composition. In particular,  $^{60}\text{Fe}$  is seen in cosmic rays (11), and anomalies in elemental iron fluxes at low energies also suggest a perturbation due to a recent event (65).

A nearby  $r$ -process event would mainly produce stable isotopes, which would be difficult to identify in deposits on the Earth or Moon, but might be detectable among the cosmic rays. Searches for heavy elements in cosmic rays have led to several intriguing new results. The Cosmic Ray Isotope Spectrometer (CRIS) recently reported data on elements with atomic number  $29 \leq Z \leq 38$  and found lower abundances of  $r$ -process species than would be expected if supernovae were their source (66). SuperTIGER has recently reported cosmic-ray abundances for heavier species as well (67, 68). The  $42 \leq Z \leq 54$  data from SuperTIGER shows anomalously high abundances, i.e., exceeding the levels of a mix of 80% solar-system-like material with a 20% admixture of supernova winds and ejecta that fits lower-mass cosmic-ray species. Some of these anomalous elements are produced mainly by the  $r$ -process, though with admixtures of  $s$ -process production. Intriguingly, the dominantly  $s$ -process species barium is not as enhanced as the other high- $Z$  elements, which may be circumstantial support for the hypothesis of a nearby  $r$ -process site (68).

Cosmic-ray measurements of other  $r$ -process species such as actinides could shed light on the nucleosynthesis pattern and thus the  $r$ -process source. If isotopic measurement were possible in future cosmic-ray experiments, observation of  $^{182}\text{Hf}$

would be particularly interesting, since it should not have significant contamination from spallation of neighboring nuclides.  $^{129}\text{I}$  and  $^{135}\text{Cs}$  would also be of interest, though contamination from spallation of Te, Xe, and Ba may be an issue.

There is compelling evidence that supernova remnants give rise to the bulk of Galactic cosmic rays, via diffusive shock acceleration (69). But this same process should act in the relativistic blast waves generated in the gamma-ray bursts and kilonovae following neutron star mergers, which therefore should also accelerate cosmic rays (70). Thus, in both the KN and SN scenarios, we expect cosmic rays to include freshly synthesized  $r$ -process material. The elemental ratios for each scenario are shaped by the prompt production as well as the spallation effects that occur as the material is ejected from the SN/KN and propagates through the ISM (71). Whether such ratios can offer an opportunity to discriminate among scenarios requires further study.

**A Strategy to Determine the Origin of Near-Earth  $^{244}\text{Pu}$ .** By combining terrestrial and lunar measurements we can hope to have information at least on the broad time history and overall fluence of  $^{60}\text{Fe}$  as produced in multiple supernovae, and separately the time history and fluence of  $^{244}\text{Pu}$ , probably  $^{129}\text{I}$ , and possibly  $^{182}\text{Hf}$ . This will give insight into the origin of the  $r$ -process signal in radioisotopes, and thus open a new window into the astrophysics site of the  $r$ -process. We distinguish three possible cases.

- No pulse coincidence: If  $^{244}\text{Pu}$  has a time history distinct from the  $^{60}\text{Fe}$  pulses, this would point to a different origin, likely a kilonova that seeded the Local Bubble. Here the transport to Earth would not be coincident with the SN blasts and imply that the  $r$ -process-bearing dust moves independently in the bubble interior (as in our simple version of the two-step model);
- One pulse coincidence: If  $^{244}\text{Pu}$  and other  $r$ -process radioisotopes trace one (and only one) of the  $^{60}\text{Fe}$  pulses, this points to a supernova origin of the  $r$  process, and indeed a supernova origin of  $r$ -process actinides. This would have major implications for supernova physics, and for Galactic chemical evolution. In this case the  $^{244}\text{Pu}/^{60}\text{Fe}$  ratio would probe supernova actinide production;
- Two pulse coincidences: If  $^{244}\text{Pu}$  traces *both*  $^{60}\text{Fe}$  pulses, this would either (a) require that both supernovae produced  $r$ -process actinides, which would challenge the prevailing SN nucleosynthesis models, or that (b) the Local Bubble was seeded with recent  $r$ -process events whose radioisotopes were later delivered by the supernova blasts. This would point to a kilonova origin for  $r$ -process actinides. As we have shown, radioisotope ratios,  $r/^{244}\text{Pu}$ , can distinguish these cases.

Lower  $r/^{244}\text{Pu}$  ratios would point to an kilonova scenario as in (a). The two supernovae could have different  $^{60}\text{Fe}$

yields, so the two  $r/^{60}\text{Fe}$  ratios could vary (although (30) find that  $^{60}\text{Fe}/^{244}\text{Pu}$  is consistent with a constant ratio). But the common origin of the  $r$ -process species means that the ratios among the  $r$ -process species should be the same (within errors) for the two pulses. Thus consistency of the  $^{129}\text{I} : ^{182}\text{Hf} : ^{244}\text{Pu}$  ratios would provide a check on this scenario.

High measured  $r/^{244}\text{Pu}$  ratios would indicate supernova origins as in (b). This would be quite unexpected, as it would require that the Local Bubble harbored at least two  $r$ -process supernovae, and these were among the nearest events, suggesting that SNe produce the  $r$ -process much more commonly than has been thought. The  $^{60}\text{Fe}/^{244}\text{Pu}$  and  $^{129}\text{I} : ^{182}\text{Hf} : ^{244}\text{Pu}$  ratios would probe the uniformity of the  $r$ -process synthesis in these two explosions.

In all cases, the  $r/^{244}\text{Pu}$  ratios probe in detail the nucleosynthesis and dust formation of these species. If the dust formation properties are similar, then these species probe  $r$ -process pattern in the source identified by the time history results. In particular,  $^{129}\text{I}$  probes the production of the second  $r$ -process peak, while  $^{182}\text{Hf}$  probes the base of the third peak. Observational data linking the second and third  $r$ -process peaks from the same source are limited, in large part because second peak elements such as Te can only be spectroscopically identified in the UV. There are hints in these data that Te production may be more strongly correlated with the first  $r$ -process peak than the third (72). A coincident detection of  $^{129}\text{I}$  and  $^{182}\text{Hf}$ , therefore, would add to this limited body of data and offer an independent test of this intriguing suggestion. †

It is worth noting that, as we have seen, the one reported measurement of  $^{129}\text{I}$  in lunar regolith (61) apparently rules out much of the SN parameter space. This is also apparently the case for the one reported  $^{129}\text{I}$  measurement in deep-ocean Fe-Mn crusts (29, 62), though the crust has not been independently dated. These tantalizing past results were not made with our research program in mind, and follow-up measurements are in order to confirm these hints and to better illuminate cosmogenic backgrounds. But the results in hand show that the experimental sensitivity to  $^{129}\text{I}$  already within reach can enable dedicated measurements to shed new light on the  $r$ -process.

**Conclusion and Discussion: Unearthing the Origin of  $r$ -Process Radioisotopes.** The combination of lunar and deep-sea probes of radioisotopes are complementary, and may reveal their origin.

- Deep-sea crusts characterize the broad time history, e.g., the number of  $^{60}\text{Fe}$  pulses. Future  $^{244}\text{Pu}$  measurements with better time resolution can test the coincidence with  $^{60}\text{Fe}$  and probe for events  $\gtrsim 8$  Myr ago. Searches for other  $r$ -process species test the SN and KN models, and the  $^{129}\text{I}$  radioisotope has already been found in one crust.
- Deep-sea sediments give high-resolution time history, determining the timescales and, with improved sensitivity, the time profiles of the pulses.

† Future searches for radioactive decay lines from  $r$ -process radioisotopes by next generation MeV gamma-ray observatories such as COSI (<https://cosi.ssl.berkeley.edu>), AMEGO (<https://asd.gsfc.nasa.gov/amego/>) and MeVGRO (<https://indico.icranet.org/event/1/contributions/777/>) may also provide information on near-earth nucleosynthesis events (e.g., 73).

- Lunar measurements avoid anthropogenic contamination, and so would offer important confirmation of the  $^{244}\text{Pu}$  detections, and are complementary to deep-sea crusts as sites for other  $r$ -process species that can discriminate between the SN and KN scenarios. But regolith abundances require careful accounting for cosmic-ray production via measurements of target abundances and accompanying cosmogenic-dominated radioisotopes that encode exposure doses.
- Lunar surface density measurements give the total fluence at Earth, summing over all events and avoiding uncertainties associated with terrestrial uptake factors.
- The lunar depth profile combined with a gardening model can give timing information or, vice versa, its combination with sediment data would give a new constraint on gardening. It is possible that the depth profile might give indications of multiple events, but local stochastic variations might make this difficult.
- Comparing the  $^{60}\text{Fe}/^{244}\text{Pu}$  and  $r/^{244}\text{Pu}$  in deep-sea crusts and sediments probes uptake and helps determine the fluence independently of the lunar measurements.
- Comparing the lunar  $^{60}\text{Fe}/^{244}\text{Pu}$  and  $r/^{244}\text{Pu}$  with those in crusts probes uptake, and comparison with sediment data probes non-uniformity of terrestrial deposition and possibly lunar impact losses and thus impactor velocity.

The models that indicate  $> 10$  supernovae formed the Local Bubble (46, 47) suggest that there may be pulses of radioisotopes still earlier than SN Mio at 7 Myr ago. This regime is probably beyond the reach of  $^{60}\text{Fe}$  due to decay, but fortunately all of  $^{129}\text{I}$ ,  $^{182}\text{Hf}$ , and  $^{244}\text{Pu}$  can probe to 10 Myr ago and earlier, so any early  $r$ -process signal would remain. To search for a correlation with supernovae would require a long-lived radioisotope likely made in core collapse;  $^{146}\text{Sm}$  could be a candidate.

The studies recommended in this work capitalize on recent technical advances, including expanded capabilities at AMS facilities to perform high-resolution measurements and the promise of next-generation radioactive beam facilities to reduce the considerable nuclear physics uncertainties of nucleosynthetic yield estimates (74). We look forward to future studies of the deep ocean crust—including more data on the 7-Mya SN Mio and earlier samples—as well as further data from sediments and the Antarctic snow. As we have argued here, lunar samples offer a unique complement to terrestrial sources and hold the promise to distinguish among  $r$ -process production scenarios, for which we anticipate results from the sample return missions of *Chang'e* and *Artemis*.

## Materials and Methods

**Nucleosynthetic yield estimates and predicted ratios of radioisotopes.** The measured ratios of  $^{60}\text{Fe}/^{244}\text{Pu}$  and other radioisotopes reflects the interstellar fluence ratios for these species. For species of supernova origin such as  $^{60}\text{Fe}$ , we use the usual expression (1, 33) for fluence (i.e., the time-integrated flux),  $\mathcal{F}_{60} = f_{\text{Fe}} M_{\text{ej},60} e^{-t/\tau_{60}} / (4\pi A_{60} m_{\text{u}} r_{\text{SN}}^2)$ , in the case of  $^{60}\text{Fe}$ , and similar for other species. Here the dust fraction measures the portion of the  $^{60}\text{Fe}$  ejecta arriving in grains. For the fluence of an individual



species, one must specify the dust fraction as well as a distance, but *ratios* of supernova species are independent of distance; they depend only on the dust fractions and yields as well as basic nuclear properties:

$$\frac{\mathcal{F}_i}{\mathcal{F}_j} = \frac{A_j}{A_i} \frac{f_i}{f_j} \frac{M_{\text{ej},i}}{M_{\text{ej},j}} \exp[-t_i(\tau_i^{-1} - \tau_j^{-1})] \quad [1]$$

Throughout we take  $f_i/f_j = 1$ , i.e., we assume the same dust incorporation efficiency for all species of interest. Thus, for the SN (one-step) case the ratios depend only on the yields. For the KN case, we use the two-step model from (29), with a KN distance of 1000 pc.

Our  $r$ -process nucleosynthesis calculations are made using the nuclear reaction network code Portable Routines for Integrated nucleoSynthesis Modeling (PRISM) (75, 76), as implemented in (29), with baseline nuclear data from (77) and (78) (FRDM+QRPA), and variations in the masses (79) (HFB),  $\beta$ -decay rates (80) (MKT), and fission yields (81).

To combine the  $r$ -process  $^{60}\text{Fe}$  with the ordinary supernova production requires that we specify the  $^{60}\text{Fe}$  mass yields for both ordinary and  $r$ -process synthesis. Turning first to supernova yields, gamma-ray line observations provide an observational indication of the mean  $^{60}\text{Fe}$  yield. Given a Galactic steady-state  $^{60}\text{Fe}$  mass  $M_{60,\text{ss}} = 2.85 M_\odot$  (82), and a core-collapse supernova rate  $R_{\text{SN}} = 1.7 \text{ events/century}$  (83), the mean  $^{60}\text{Fe}$  yield is  $M_{\text{ej},60} = M_{60,\text{ss}}/\tau_{60} R_{\text{SN}} = 4.5 \times 10^{-5} M_\odot$ , where  $\tau_{60}$  is the  $^{60}\text{Fe}$  lifetime; the uncertainty in this mean yield is at least a factor of 2. However, nucleosynthesis calculations suggest that  $^{60}\text{Fe}$  yields from individual SNe span a wide range, varying sensitively and non-monotonically with progenitor mass. Yields in ref. (40) lie in the range  $(4 \times 10^{-6}, 3 \times 10^{-4}) M_\odot$ , which includes the calculations of (41) and model w of (42). We thus adopt an ‘ordinary’  $^{60}\text{Fe}$  yield of  $M_{\text{ej},60} = 10^{-4.5 \pm 1} M_\odot$ . The models labeled ‘SA+SNnonr’ and ‘SB+SNnonr’ in Fig. 1 include this  $^{60}\text{Fe}$  yield. Similarly, the yields of  $^{93}\text{Zr}$  from ordinary (non- $r$ -process) supernova explosions are in the range  $(1.4 \times 10^{-9}, 2.4 \times 10^{-7}) M_\odot$  (41, 42), thus an ‘ordinary’  $^{93}\text{Zr}$  yield of  $M_{\text{ej},93} = 10^{-7.5 \pm 1} M_\odot$  is included in the models labeled ‘SA+SNnonr’ and ‘SB+SNnonr’ in Fig. 2.

For the  $r$ -process mass yields, we adopt ref.(29)’s estimate for both the SN and KN models:  $M_{\text{ej},r}(\text{SA, SB, KA, KB}) = (1.37 \times 10^{-5}, 3.0 \times 10^{-2}, 1.76 \times 10^{-2}, 7.00 \times 10^{-3}) M_\odot$ . The  $^{244}\text{Pu}$  and  $^{60}\text{Fe}$   $r$ -process mass yields are then  $M_{\text{ej},244} = A_{244} Y_{244} M_{\text{ej},r}$ ,  $M_{\text{ej},60} = A_{60} Y_{60} M_{\text{ej},r}$ . We add the two  $^{60}\text{Fe}$  yields for the SN models.

For  $^{244}\text{Pu}$ , we use the observed interstellar  $^{244}\text{Pu}$  flux (30) to determine the fluence  $F_{244} = \Phi_{244}^{\text{interstellar}} \Delta t$ , where  $\Delta t$  is the time span of the measurement interval. The  $r$ -process contribution to  $^{60}\text{Fe}$  then follows as  $F_{60,r} = f_{\text{Fe}}/f_{\text{Pu}} (^{60}\text{Fe}/^{244}\text{Pu})_r F_{244}$ , where  $(^{60}\text{Fe}/^{244}\text{Pu})_r$  is the model abundance ratio by number calculated above. The other  $r$ -process species have fluence ratios just given by their production number ratios, again assuming dust fractions  $f_i/f_{\text{Pu}} = 1$ .

### The Cosmic-Ray Background of Radioisotopes in Lunar Regolith.

Cosmic rays with MeV energies and above undergo reactions in the lunar regolith and produce radioisotopes. This cosmogenic component creates an irreducible background for radioisotopes produced in astrophysical explosions. Here we determine the level of this background, and outline a strategy to use regolith measurements to disentangle the cosmogenic background from the SN or KN signal we seek. We also estimate the level of *destruction* of SN and KN radioisotopes by cosmic-ray interactions.

**Cosmic-Ray Production of Radioisotopes in Lunar Regolith.** Cosmic rays incident on the lunar regolith create showers of secondary protons and neutrons. These cascades are the most intense at depths around  $\sim (10, 30)$  cm below the surface for protons and neutrons respectively, and are attenuated below (50, 52, 84). For the 10-100 MeV energies most important for our purposes, the neutron fluxes are larger by more than an order of magnitude because neutrons do not suffer the Coulomb losses that stop the protons. These secondary particles react with regolith material to produce radioisotopes, whose abundance is a background that competes with our supernova or kilonova signal.

For radioisotope  $i$  produced by cosmic-ray interactions of target nucleus  $j$ , the production rate per unit volume is

$$q_i = \langle \Phi_p \sigma_{p \rightarrow i} + \Phi_n \sigma_{n \rightarrow i} \rangle n_j = \Gamma_{j \rightarrow i}^{\text{CR}} n_j = \Gamma_{j \rightarrow i}^{\text{CR}} \frac{\rho}{A_j m_u} X_j. \quad [2]$$

This is the product of the target number density  $n_j$  and the cosmic-ray interaction the rate per target  $\langle \Phi \sigma \rangle$ , with  $\Phi$  the cosmic-ray flux and  $\sigma$  the cross section for producing species  $i$ , summed over cosmic-ray protons and neutrons, and averaged over the cosmic-ray spectrum *in situ*. We see that the cosmic-ray production is proportional to the target abundance, i.e., the mass fraction:  $q_i \propto n_j \propto \rho_j \propto X_j$ .

The production competes with the radioactive decay at rate per volume, or activity  $a_i = n_i/\tau_i$ . The production and decay rates are driven to an equilibrium where  $a_i^{\text{eq}} = q_i$ . This state is reached over a timescale of order  $\tau_i$ , i.e., within a few Myr in our case, and so should be a good approximation for our purposes. Thus we expect the cosmogenic species to have equilibrium abundances given by  $n_i^{\text{eq}} = q_i \tau_i$ .

Because cosmic-ray production is proportional to the target abundance, cosmogenic radioisotope measurements are often reported as a decay rate per target mass, i.e., the specific activity

$$\mathcal{A}_{i|j} = \frac{a_i}{\rho_j} = \frac{n_i}{\tau_i X_j \rho} \stackrel{\text{eq}}{=} \frac{\Phi \sigma}{A_j m_u}, \quad [3]$$

where  $\tau_i$  is the mean life of  $i$ , and  $X_j = \rho_j/\rho$  is the mass fraction of the target. This ratio depends only on the cosmic-ray flux in the regolith (intensity and spectrum), and the cross sections for radioisotope production. We can thus find the number of cosmogenic radioisotope atoms per unit mass as

$$\begin{aligned} \frac{n_i^{\text{CR}}}{\rho} &= \mathcal{A}_{i|j} X_j \tau_i \\ &= 5.3 \times 10^5 \text{ atoms/g} \left( \frac{X_j}{100 \text{ ppm}} \right) \left( \frac{\tau_i}{10 \text{ Myr}} \right) \left( \frac{\mathcal{A}_{i|j}}{1 \text{ dpm/kgj}} \right) \end{aligned} \quad [4]$$

where  $\text{dpm/kgj} = \text{decay min}^{-1} (\text{kg j})^{-1}$ . Note that a mass fraction of 1 ppm corresponds to  $X(1 \text{ ppm}) = 10^{-6}$ , so our fiducial value in eq. (4) is for  $X(100 \text{ ppm}) = 10^{-4}$ .

We can use eq. (4) to infer the cosmic-ray backgrounds for our radioisotopes of interest, and compare with the levels we predict for the signals from nearby explosions. For example, the cosmic-ray background for  $^{129}\text{I}$  is mainly from cosmic-ray interactions with barium and tellurium isotopes. The tellurium abundance is generally small ( $X_{\text{Te}} \leq 10^{-6}$ ) in the lunar regolith, while the barium abundances in the lunar soil span  $X_{\text{Ba}} \sim 42 - 850 \text{ ppm}$  §. Adopting  $\mathcal{A}_{129\text{I}|\text{Ba}} = 1.5 \text{ dpm/kg Ba}$  (85), we estimate the cosmogenic  $^{129}\text{I}$  atoms per unit mass to be  $\sim 2.4 \times 10^7 \text{ atoms/g}$ , shown as the  $^{129}\text{I}$  background in Fig. 3, along with values from measurements of  $^{129}\text{I}$  in a lunar rock (58) and regolith (61); for these we use a barium mass fraction  $X_{\text{Ba}} = 389 \text{ ppm}$  (86). The background is proportional to the barium abundance and thus samples with smaller  $X_{\text{Ba}}$  would be ideal.

The main target isotope for the cosmogenic production of  $^{182}\text{Hf}$  is the tungsten isotope  $^{186}\text{W}$ . The TALYS (87) ¶ theoretical cross section values for cosmic rays interacting with this isotope are  $\sigma(p + ^{186}\text{W}) \simeq 0.9 \text{ mb}$ , and  $\sigma(n + ^{186}\text{W}) \simeq 2 \text{ mb}$ . We combine these with a tungsten regolith mass fraction of  $X_{\text{W}} = 10^{-6}$  (88), isotope fraction  $^{186}\text{W}/\text{W} = 0.28$ , and a cosmic-ray flux in the regolith of  $\Phi_N = 4 \text{ cm}^{-2}\text{s}^{-1}$ . This gives the  $^{182}\text{Hf}$  background shown as the horizontal line in Fig. 3.

In general, the lunar soil will contain both an astrophysical signal from a nearby explosion (SN or KN) and a cosmogenic background. For radioisotope  $i$ , the number density in a sample  $n_i^{\text{obs}} = n_i^* + n_i^{\text{CR}}$  sums the two components, and so we have

$$\left( \frac{e_i}{\rho} \right)_{\text{obs}} = \left( \frac{n_i^*}{\rho} \right) + \left( \frac{n_i^{\text{CR}}}{\rho} \right) \quad [5]$$

$$= \left( \frac{\mathcal{F}_i^*}{\rho h_{\text{mix}}} \right) + \frac{\Gamma_{j \rightarrow i}^{\text{CR}} \tau_i}{A_j m_u} X_j \quad [6]$$

$$= \left( \frac{\mathcal{F}_i^*}{\rho h_{\text{mix}}} \right) + \mathcal{A}_{i|j} \tau_i X_j, \quad [7]$$

§ <https://www.lpi.usra.edu/lunar/samples/>

¶ [https://tendl.web.psi.ch/tendl\\_2021/talys.html](https://tendl.web.psi.ch/tendl_2021/talys.html)



where the last equation assumes that the fluence  $\mathcal{F}_i^*$  of the isotope from a nearby explosion is mixed over a depth  $h_{\text{mix}}$ .

**Strategy to distinguish the astrophysical signal from background in lunar regolith sample.** Equation (6) shows that a potential signal from an astrophysical explosion will be mixed with a cosmogenic background, and we thus require a means of separating these components. The available samples of lunar regolith and lunar soil show variations in elemental abundances. This suggests a simple strategy: search for species  $i$  of interest in samples with low target abundances  $X_j$ , and the plot  $n_i/\rho$  vs  $X_j$ . One can then find both the slope and intercept, which encode the cosmic-ray and astrophysical components respectively. This simple approach faces the problem that regolith samples at different depths experience different mixing (49) and different cosmic-ray exposure (50, 52, 84). This can introduce large spreads in both the slope and intercept of our linear trend of  $n_i/\rho$  vs  $X_j$ . We have verified with lunar and meteoritic data that the  $n(^{60}\text{Fe})/\rho$  versus the target  $X_{\text{Ni}}$  abundance that the observed trend is too noisy for a robust inference of the astrophysical component. The uncertainties in the linear slope are large and consistent with zero.

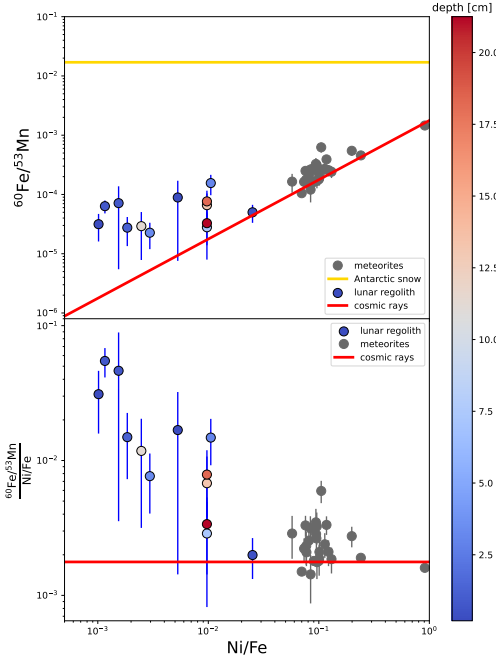


**Fig. 4.** Ratio of  $^{60}\text{Fe}/^{53}\text{Mn}$  for meteorites and lunar regolith. Panel (a): Ratio of  $^{60}\text{Fe}/^{53}\text{Mn}$  versus  $\text{Ni}/\text{Fe}$ . The linear trend for cosmic-ray production shown as a line, and the excess in regolith indicates another source. Panel (b): Ratio of  $(^{60}\text{Fe}/^{53}\text{Mn})/(\text{Ni}/\text{Fe})$  versus  $\text{Ni}/\text{Fe}$ : the cosmic-ray trend is horizontal, and the excess above it indicates the importance of an additional source.

To overcome the problem of different cosmic-ray exposures for different samples, one can measure another radioisotope in the same samples—a species that is only of cosmogenic origin. Fimiani et al. (ref. (10)) successfully adopted this approach, measuring not only  $^{60}\text{Fe}$  in lunar regolith, but also  $^{53}\text{Mn}$  that has a high cosmogenic abundance due to the large abundance of its target nuclei such as  $^{56}\text{Fe}$ . Here we use their lunar and meteoritic data to illustrate this procedure. Our analysis elaborates the procedure discussed recently by Koll et al. in ref. (59).

We consider two radioisotopes: one denoted by  $i$  that has or may have a supernova component, e.g.,  $^{60}\text{Fe}$ ,  $^{244}\text{Pu}$ ,  $^{129}\text{I}$ , etc. The other is dominated by cosmic-ray production; we denote this by  $k$  and have in mind  $^{53}\text{Mn}$ . Thus both species obey eq. (6), but one

has no discernible astrophysical component: we use this cosmogenic species  $k$  as the tracer. We write the number of radioisotope atoms per sample mass as  $y_i = n_i/\rho$ , so that  $y_i = y_i^{\text{CR}} + y_i^*$ , while  $y_k = y_k^{\text{CR}}$ . For the cosmic-ray components  $y_i^{\text{CR}} = \Phi_i \sigma_{j \rightarrow i} y_j \tau_i = \tau_i \mathcal{A}_{i|j} X_j / A_j m_u$ , with a similar expression for species  $k$ . Using the  $^{60}\text{Fe}$  and  $^{53}\text{Mn}$  system as an example, we have

$$\frac{^{60}\text{Fe}}{^{53}\text{Mn}} = \frac{y_i}{y_k} = \frac{n_i}{n_k} \quad [8]$$

$$= \frac{\sigma_{j \rightarrow i} \tau_i y_j}{\sigma_{\ell \rightarrow k} \tau_j y_\ell} + \frac{y_i^*}{y_k^{\text{CR}}} \quad [9]$$

$$= \frac{\sigma_{\text{Ni} \rightarrow ^{60}\text{Fe}} \tau_{60}}{\sigma_{\text{Fe} \rightarrow ^{53}\text{Mn}} \tau_{53}} \left( \frac{\text{Ni}}{\text{Fe}} \right) + \frac{1}{\Phi \sigma_{\text{Fe} \rightarrow ^{53}\text{Mn}}} \frac{^{60}\text{Fe}^*}{\text{Fe}}. \quad [10]$$

We see that a plot of  $^{60}\text{Fe}/^{53}\text{Mn}$  versus  $\text{Ni}/\text{Fe}$  should be linear with zero intercept if there is no supernova component, with a slope that only depends on the ratio of the  $\sigma\tau$  values for the two species, not the cosmic-ray flux.

Figure 4 plots  $^{60}\text{Fe}/^{53}\text{Mn}$  versus  $\text{Ni}/\text{Fe}$  for both lunar regolith samples that should contain supernova  $^{60}\text{Fe}$ , and for meteorites that should not (10, 59). We see that the meteoritic data falls on a line with nonzero slope, indicating the presence of correlated cosmogenic production of both  $^{60}\text{Fe}$  and  $^{53}\text{Mn}$ . The presence of a positive intercept points to a supernova component, at a level that depends on the  $^{60}\text{Fe}^*/\text{Fe}_{\text{regolith}}$  mixing of SN material in the regolith, as well as the cosmic-ray exposure  $\Phi \sigma_{53} \tau_{53}$ .

We can adapt this strategy to analyze the  $r$ -process radioisotopes with future lunar measurements. Along with these species of interest, it is important to measure at least one cosmogenic-dominated radioisotope such as  $^{53}\text{Mn}$ , but it would be of interest to measure others as well such as  $^{26}\text{Al}$ , which is abundantly produced from spallation of silicon isotopes such as  $^{28}\text{Si}$ , as well as other examples, particularly those with lifetimes comparable to the species of interest.

Note that we have assumed that the cosmic-ray tracer species,  $^{53}\text{Mn}$  in our example, does not have an appreciable SN contribution in the regolith. In fact, SN production of  $^{53}\text{Mn}$  should occur, and ref. (89) report evidence for it in a Fe-Mn crust. But in this crust  $^{53}\text{Mn}$  is still dominated by the cosmogenic component, which comes from interplanetary dust infall on Earth. We find that in a lunar sample the cosmogenic  $^{53}\text{Mn}$  signal should dominate even more because the  $^{53}\text{Mn}$  production in the regolith column will far exceed the accreted dust fluence (90). Thus,  $^{53}\text{Mn}$  can effectively be treated as purely of cosmic-ray origin.

**Cosmic-Ray Destruction of Radioisotopes in Lunar Regolith.** Cosmic rays will also interact with the radioisotopes deposited by nearby explosions, converting them to other nuclides. This process reduces the signal we seek, and so is important to estimate. Cosmic-ray destruction of radioisotopes occurs mainly through spallation reactions.

We have examined destruction rates of  $^{60}\text{Fe}$ ,  $^{129}\text{I}$  and  $^{244}\text{Pu}$  by cosmic-ray proton and neutron spallation on the lunar regolith. In general, the spallation (or inelastic) cross section values for these isotopes from TALYS (87)<sup>||</sup> are  $\sigma_{\text{spall}} \lesssim O(10^4)$  mb at maximum, and in the regolith the cosmic-ray proton flux from 10–100 MeV is  $\Phi_p \lesssim O(10^{-1}) \text{ cm}^{-2} \text{ s}^{-1}$  while the neutron flux at the same energies is  $\Phi_n \lesssim O(10^0) \text{ cm}^{-2} \text{ s}^{-1}$  (84). The destruction rate is therefore at most is about  $\Gamma_{\text{inel}} = (\Phi_p + \Phi_n) \sigma_{\text{inel}} \lesssim O(10^{-22}) \text{ s}^{-1}$ . This is far less than the radioactive decay rate of these isotopes  $1/\tau_i > 10^{-16} \text{ s}^{-1}$  (take  $^{244}\text{Pu}$  for example,  $\Gamma_{244+n} \tau_{244} \sim 4 \times 10^{-8} \ll 1$ ). Thus, radioactive decay overwhelmingly dominates the losses of these species, as we have assumed throughout. Consequently the cosmic-ray destruction rates can be ignored for the lunar measurements of these isotopes.

**ACKNOWLEDGMENTS.** We are grateful for illuminating discussions with Terri Brandt and Brian Rauch about SuperTIGER and cosmic rays, and to Toni Wallner and Dominik Koll for discussions of their work. X.W., R.S., and B.D.F. acknowledge many useful discussions in the INT-21-3 workshop on cosmic radioisotopes sponsored by the Institute for Nuclear Theory. The work of X.W. was

<sup>||</sup> [https://tendl.web.psi.ch/tendl\\_2021/talys.html](https://tendl.web.psi.ch/tendl_2021/talys.html)

supported by the U.S. National Science Foundation (NSF) under grants No. PHY-1630782 and PHY-2020275 for the Network for Neutrinos, Nuclear Astrophysics, and Symmetries (N3AS) and by the Heising-Simons Foundation under award 00F1C7. The work of A.M.C. was supported by the U.S. Nuclear Regulatory Commission Award 31310019M0037 and the National Science Foundation under grant number PHY-2011890. The work of J.E. was supported partly by the United Kingdom STFC Grant ST/T000759/1 and partly by the Estonian Research Council via a Mobilitas Pluss grant. The work of A.F.E. and B.D.F. was supported by the NSF under grant number AST-2108589. The work of J.A.M. was supported by the Future Investigators in NASA Earth and Space Science and Technology (FINESST) program under grant number NNH19ZDA001N-FINESST. The work of R.S. was supported by N3AS as well as the U.S. Department of Energy under Contract Nos. DE-FG02-95-ER40934 and LA22-ML-DE-FOA-2440.

1. J Ellis, BD Fields, DN Schramm, Geological Isotope Anomalies as Signatures of Nearby Supernovae. *ApJ* **470**, 1227 (1996).
2. MA Ruderman, Possible consequences of nearby supernova explosions for atmospheric ozone and terrestrial life. *Science* **184**, 1079–1081 (1974).
3. J Ellis, DN Schramm, Could a nearby supernova explosion have caused a mass extinction? *Proc. Natl. Acad. Sci.* **92**, 235–238 (1995).
4. K Knie, et al., Indication for Supernova Produced Fe-60 Activity on Earth. *Phys. Rev. Lett.* **83**, 18–21 (1999).
5. K Knie, et al.,  $^{60}\text{Fe}$  Anomaly in a Deep-Sea Manganese Crust and Implications for a Nearby Supernova Source. *Phys. Rev. Lett.* **93**, 171103 (2004).
6. C Fitoussi, et al., Search for supernova-produced Fe-60 in a marine sediment. *Phys. Rev. Lett.* **101**, 121101 (2008).
7. A Wallner, et al., Recent near-Earth supernovae probed by global deposition of interstellar radioactive  $^{60}\text{Fe}$ . *Nature* **532**, 69–72 (2016).
8. P Ludwig, et al., Time-resolved 2-million-year-old supernova activity discovered in earth's microfossil record. *Proc. Natl. Acad. Sci.* **113**, 9232–9237 (2016).
9. A Wallner, et al.,  $^{60}\text{Fe}$  deposition during the late Pleistocene and the Holocene echoes past supernova activity. *Proc. Natl. Acad. Sci.* **117**, 21873–21879 (2020).
10. L Fimiani, et al., Interstellar  $^{60}\text{Fe}$  on the Surface of the Moon. *Phys. Rev. Lett.* **116**, 151104 (2016).
11. WR Binns, et al., Observation of the  $^{60}\text{Fe}$  nucleosynthesis-clock isotope in galactic cosmic rays. *Science* **352**, 677–680 (2016).
12. D Koll, et al., Interstellar  $^{60}\text{Fe}$  in Antarctica. *Phys. Rev. Lett.* **123**, 072701 (2019).
13. M Paul, et al., Experimental Limit to Interstellar  $^{244}\text{Pu}$  Abundance. *ApJL* **558**, L133–L135 (2001).
14. C Wallner, et al., Supernova produced and anthropogenic  $^{244}\text{Pu}$  in deep sea manganese encrustations. *New Astron. Rev.* **48**, 145–150 (2004).
15. G Raisbeck, et al., A search for supernova produced  $^{244}\text{Pu}$  in a marine sediment. *Nucl. Instruments Methods Phys. Res. B* **259**, 673–676 (2007).
16. A Wallner, et al., Abundance of live  $^{244}\text{Pu}$  in deep-sea reservoirs on Earth points to rarity of actinide nucleosynthesis. *Nat. Commun.* **6**, 5956 (2015).
17. EM Burbidge, GR Burbidge, WA Fowler, F Hoyle, Synthesis of the Elements in Stars. *Rev. Mod. Phys.* **29**, 547–650 (1957).
18. BP Abbott et al., Gw170817: Observation of gravitational waves from a binary neutron star inspiral. *Phys. Rev. Lett.* **119**, 161101 (2017).
19. BP Abbott, et al., Multi-messenger Observations of a Binary Neutron Star Merger. *ApJL* **848**, L12 (2017).
20. PS Cowperthwaite et al., The electromagnetic counterpart of the binary neutron star merger ligo/virgo gw170817. ii. uv, optical, and near-infrared light curves and comparison to kilonova models. *ApJL* **848**, L17 (2017).
21. D Kasen, B Metzger, J Barnes, E Quataert, E Ramirez-Ruiz, Origin of the heavy elements in binary neutron-star mergers from a gravitational-wave event. *Nature* **551**, 80–84 (2017).
22. IU Roederer, JE Lawler, Detection of Elements at All Three r-process Peaks in the Metal-poor Star HD 160617. *ApJ* **750**, 76 (2012).
23. EM Holmbeck, et al., The R-Process Alliance: 2MASS J09544277+5246414, the Most Actinide-enhanced R-II Star Known. *ApJL* **859**, L24 (2018).
24. VM Placco, et al., The R-process Alliance: The Peculiar Chemical Abundance Pattern of RAVE J183013.5-455510. *ApJ* **897**, 78 (2020).
25. JJ Cowan, FK Thielemann, JW Truran, The r-process and nucleochronology. *Phys. Reports* **208**, 267–394 (1991).
26. M Arnould, S Goriely, K Takahashi, The r-process of stellar nucleosynthesis: Astrophysics and nuclear physics achievements and mysteries. *Phys. Reports* **450**, 97–213 (2007).
27. JJ Cowan, et al., Origin of the heaviest elements: The rapid neutron-capture process. *Rev. Mod. Phys.* **93**, 015002 (2021).
28. T Kajino, et al., Current status of r-process nucleosynthesis. *Prog. Part. Nucl. Phys.* **107**, 109–166 (2019).
29. X Wang, et al., r-Process Radioisotopes from Near-Earth Supernovae and Kilonovae (2021).
30. A Wallner, et al.,  $^{60}\text{Fe}$  and  $^{244}\text{Pu}$  deposited on Earth constrain the r-process yields of recent nearby supernovae. *Science* **372**, 742–745 (2021).
31. H Zinnecker, HW Yorke, Toward Understanding Massive Star Formation. *ARA@AND@A* **45**, 481–563 (2007).
32. AF Ertel, BJ Fry, BD Fields, J Ellis, Supernova Dust Evolution Probed by Deep-Sea  $^{60}\text{Fe}$  Time History. *arXiv e-prints* p. arXiv:2206.06464 (2022).
33. BJ Fry, BD Fields, JR Ellis, Astrophysical Shrapnel: Discriminating among Near-Earth Stellar Explosion Sources of Live Radioactive Isotopes. *ApJ* **800**, 71 (2015).
34. Y Zhu, et al., Californium-254 and Kilonova Light Curves. *ApJL* **863**, L23 (2018).
35. A Arcones, HT Janka, Nucleosynthesis-relevant conditions in neutrino-driven supernova outflows. II. The reverse shock in two-dimensional simulations. *A@AND@A* **526**, A160 (2011).
36. P Mösta, et al., r-process Nucleosynthesis from Three-dimensional Magnetorotational Core-collapse Supernovae. *ApJ* **864**, 171 (2018).
37. L Bovard, et al., r-process nucleosynthesis from matter ejected in binary neutron star mergers. *Phys. Rev. D* **96**, 124005 (2017).
38. O Just, A Bauswein, R Ardevol Pulpillo, S Goriely, HT Janka, Comprehensive nucleosynthesis analysis for ejecta of compact binary mergers. *MNRAS* **448**, 541–567 (2015).
39. M Limongi, A Chieffi, The Nucleosynthesis of  $^{26}\text{Al}$  and  $^{60}\text{Fe}$  in Solar Metallicity Stars Extending in Mass from 11 to 120  $M_{\text{Solar}}$ : The Hydrostatic and Explosive Contributions. *ApJ* **647**, 483–500 (2006).
40. T Sukhbold, T Ertl, SE Woosley, JM Brown, HT Janka, Core-collapse Supernovae from 9 to 120 Solar Masses Based on Neutrino-powered Explosions. *ApJ* **821**, 38 (2016).
41. M Limongi, A Chieffi, Presupernova Evolution and Explosive Nucleosynthesis of Rotating Massive Stars in the Metallicity Range  $-3 \leq [\text{Fe}/\text{H}] \leq 0$ . *ApJS* **237**, 13 (2018).
42. S Curtis, et al., PUSHing Core-collapse Supernovae to Explosions in Spherical Symmetry. III. Nucleosynthesis Yields. *ApJ* **870**, 2 (2019).
43. BJ Fry, BD Fields, JR Ellis, Magnetic Imprisonment of Dusty Pinballs by a Supernova Remnant. *ApJ* **894**, 109 (2020).
44. EM Holmbeck, et al., The R-Process Alliance: Fourth Data Release from the Search for R-process-enhanced Stars in the Galactic Halo. *ApJS* **249**, 30 (2020).
45. AP Ji, A Frebel, A Chiti, JD Simon, R-process enrichment from a single event in an ancient dwarf galaxy. *Nature* **531**, 610–613 (2016).
46. D Breitschwerdt, et al., The locations of recent supernovae near the Sun from modelling  $^{60}\text{Fe}$  transport. *Nature* **532**, 73–76 (2016).
47. MM Schulerich, D Breitschwerdt, J Feige, C Dettbarn, Numerical studies on the link between radioisotopic signatures on Earth and the formation of the Local Bubble - I.  $^{60}\text{Fe}$  transport to the solar system by turbulent mixing of ejecta from nearby supernovae into a locally homogeneous interstellar medium. *Astron. Astrophys.* **604**, A81 (2017).
48. DE Gault, F Hoerz, DE Brownlee, JB Hartung, Mixing of the lunar regolith. *Lunar Planet. Sci. Conf. Proc.* **3**, 2365–2386 (1974).
49. ES Costello, RR Ghent, PG Lucey, The mixing of lunar regolith: Vital updates to a canonical model. *Icarus* **314**, 327–344 (2018).
50. RC Reedy, JR Arnold, Interaction of solar and galactic cosmic-ray particles with the Moon. *J. Geophys. Res.* **77**, 537 (1972).
51. S Vogt, GF Herzog, RC Reedy, Cosmogenic nuclides in extraterrestrial materials. *Rev. Geophys.* **28**, 253–275 (1990).
52. I Leya, S Neumann, R Wieler, R Michel, The production of cosmogenic nuclides by GCR-particles for 2 pi exposure geometries. *Meteorit. Planet. Sci.* **36**, 1547–1561 (2001).
53. I Leya, J Hirtz, JC David, Galactic Cosmic Rays, Cosmic-Ray Variations, and Cosmogenic Nuclides in Meteorites. *ApJ* **910**, 136 (2021).
54. Y Qian, et al., China's chang'e-5 landing site: Geology, stratigraphy, and provenance of materials. *Earth Planet. Sci. Lett.* **561**, 116855 (2021).
55. M Smith, et al., The artemis program: An overview of nasa's activities to return humans to the moon in 2020. *IEEE Aerospace Conference*. pp. 1–10 (2020).
56. ES Costello, RR Ghent, M Hirabayashi, PG Lucey, Impact gardening as a constraint on the age, source, and evolution of ice on mercury and the moon. *J. Geophys. Res. Planets* **125**, e2019JE006172 (2020).
57. K Nishiizumi, PW Kubik, P Sharma, JR Arnold,  $^{127}\text{I}$  depth profiles in cores from Jilin and the Moon. *Meteoritics* **24**, 310 (1989).
58. K Nishiizumi, D Elmore, M Honda, JR Arnold, HE Gove, Measurements of  $^{129}\text{I}$  in meteorites and lunar rock by tandem accelerator mass spectrometry. *Nature* **305**, 611–612 (1983).
59. D Koll, et al., The Dyadic Radionuclide System  $^{60}\text{Fe} / ^{53}\text{Mn}$  to Distinguish Interstellar from Interplanetary  $^{60}\text{Fe}$  in *European Physical Journal Web of Conferences*, European Physical Journal Web of Conferences. Vol. 260, p. 11022 (2022).
60. L Ji, et al., Measurement of  $^{129}\text{I}$  in ferromanganese crust with AMS. *Acta Oceanol. Sinica* **34**, 31–35 (2015).
61. K Nishiizumi, PW Kubik, P Sharma, JR Arnold,  $^{129}\text{I}$  Depth Profiles in Cores from Jilin and the Moon in *52nd Annual Meeting of the Meteoritical Society*. Vol. 52, p. 179 (1989).
62. L Ji, G Liu, Y Huang, N Xing, Z Chen, The distribution of iodine and effects of phosphatization on it in the ferromanganese crusts from the mid-pacific ocean. *Acta Oceanol. Sinica* **34**, 13–19 (2015).
63. BJ Fry, BD Fields, JR Ellis, Radioactive Iron Rain: Transporting  $^{60}\text{Fe}$  in Supernova Dust to the Ocean Floor. *ApJ* **827**, 48 (2016).
64. M Kachelrieß, A Neronov, DV Semikoz, Cosmic ray signatures of a 2-3 Myr old local supernova. *Phys. Rev. D* **97**, 063011 (2018).
65. MJ Boschini, et al., The Discovery of a Low-energy Excess in Cosmic-Ray Iron: Evidence of the Past Supernova Activity in the Local Bubble. *ApJ* **913**, 5 (2021).
66. WR Binns, et al., The Isotopic Abundances of Galactic Cosmic Rays with Atomic Number  $29 \leq Z \leq 38$ . *Astrophys. J.* **936**, 13 (2022).
67. NE Walsh, et al., SuperTIGER Abundances of Galactic Cosmic Rays for the Atomic Number (Z) Interval 30 to 56. *PoS ICRC2021*, 118 (2021).
68. NE Walsh, SuperTIGER Elemental Abundances for the Charge Range  $41 \leq Z \leq 56$ . *Wash. Univ. Arts & Sci. Electron. Theses Diss.* **2251** (2020).
69. M Ackermann, et al., Detection of the Characteristic Pion-Decay Signature in Supernova Remnants. *Science* **339**, 807–811 (2013).
70. E Waxman, Cosmological Gamma-Ray Bursts and the Highest Energy Cosmic Rays. *Phys. Rev. Lett.* **75**, 386–389 (1995).
71. X Wang, et al., Sandblasting the r-process: Spallation of Ejecta from Neutron Star Mergers. *ApJ* **893**, 92 (2020).
72. IU Roederer, et al., The R-Process Alliance: Abundance Universality among Some Elements at and between the First and Second R-Process Peaks. *ApJ* **936**, 84 (2022).
73. X Wang, et al., MeV Gamma Rays from Fission: A Distinct Signature of Actinide Production in Neutron Star Mergers. *ApJL* **903**, L3 (2020).

74. CJ Horowitz, et al., r-process nucleosynthesis: connecting rare-isotope beam facilities with the cosmos. *J. Phys. G Nucl. Phys.* **46**, 083001 (2019).
75. MR Mumpower, et al.,  $\beta$ -delayed Fission in r-process Nucleosynthesis. *ApJ* **869**, 14 (2018).
76. TM Sprouse, MR Mumpower, R Surman, Following nuclei through nucleosynthesis: a novel tracing technique. *arXiv e-prints* (2020).
77. P Möller, AJ Sierk, T Ichikawa, H Sagawa, Nuclear ground-state masses and deformations: FRDM(2012). *At. Data Nucl. Data Tables* **109**, 1–204 (2016).
78. P Möller, MR Mumpower, T Kawano, WD Myers, Nuclear properties for astrophysical and radioactive-ion-beam applications (ii). *At. Data Nucl. Data Tables* **125**, 1–192 (2019).
79. S Goriely, N Chamel, JM Pearson, Skyrme-Hartree-Fock-Bogoliubov Nuclear Mass Formulas: Crossing the 0.6MeV Accuracy Threshold with Microscopically Deduced Pairing. *Phys. Rev. Lett.* **102**, 152503 (2009).
80. T Marketin, L Huther, G Martinez-Pinedo, Large-scale evaluation of  $\beta$ -decay rates of r-process nuclei with the inclusion of first-forbidden transitions. *Phys. Rev. C* **93**, 025805 (2016).
81. T Kodama, K Takahashi, R-process nucleosynthesis and nuclei far from the region of  $\beta$ -stability. *Nucl. Phys. A* **239**, 489–510 (1975).
82. R Diehl, et al., The Radioactive Nuclei  $^{26}\text{Al}$  and  $^{60}\text{Fe}$  in the Cosmos and in the Solar System. *arXiv e-prints* (2021).
83. K Rozwadowska, F Vissani, E Cappellaro, On the rate of core collapse supernovae in the milky way. *New Astron.* **83**, 101498 (2021).
84. R Michel, P Dragovitsch, P Cloth, G Dagge, D Filges, On the Production of Cosmogenic Nuclides in Meteoroids by Galactic Protons. *Meteoritics* **26**, 221 (1991).
85. C Schnabel, et al., Production rates and proton-induced production cross sections of 129I from Te and Ba: An attempt to model the 129I production in stony meteoroids and 129I in a Knyahinya sample. *Meteorit. & Planet. Sci.* **39**, 453–466 (2004).
86. CC Schnetzler, JA Philpotts, Alkali, alkaline earth and rare-earth element concentrations in some Apollo 12 soils, rocks, and separated phases. *Lunar Planet. Sci. Conf. Proc.* **2**, 1101 (1971).
87. AJ Koning, et al., TENDL: Complete Nuclear Data Library for Innovative Nuclear Science and Technology. *Nucl. Data Sheets* **155**, 1–55 (2019).
88. TS Kruijer, T Kleine, Tungsten isotopes and the origin of the Moon. *Earth Planet. Sci. Lett.* **475**, 15–24 (2017).
89. G Korschinek, et al., Supernova-produced  $^{53}\text{Mn}$  on earth. *Phys. Rev. Lett.* **125**, 031101 (2020).
90. SG Love, DE Brownlee, A Direct Measurement of the Terrestrial Mass Accretion Rate of Cosmic Dust. *Science* **262**, 550–553 (1993).